geosciences

MDPI

Article

A Dynamic Early Warning Model for Rainfall-Induced Landslides Coupling Slope Units and Rainfall Thresholds: A Case Study of Jinyang County, Southwest China

Feng Zhang [1,2,3], Qili Xie [1,2], Yong Zhang [1,2,*], Jinyang Li [1,2,*], Jingsong Yi [1,2], Qing He [1,2], Lu Jiang [4], Ping Wang [3] and Shilong Sun [5]

[1] Institute of Exploration Technology, Chinese Academy of Geological Sciences, Chengdu 611734, China; z13320729735@163.com (F.Z.); xieqili.l@foxmail.com (Q.X.)
[2] Engineering Technology Innovation Center for Geological Disaster Risk Prevention and Control, Ministry of Natural Resources, Chengdu 611734, China
[3] 208 Hydrogeology and Engineering Geology Team, Chongqing Bureau of Geology and Mineral Exploration and Development, Chongqing 400700, China
[4] College of Water Resources, Shenyang Agricultural University, Shenyang 110866, China; 2025220032@stu.syau.edu.cn
[5] Sichuan Huadi Construction Engineering Co., Ltd., Chengdu 610081, China; ssl20001235@163.com
* Correspondence: gyszhangyong@mail.cgs.gov.cn (Y.Z.); 15882017032@163.com (J.L.); Tel.: +86-13880616238 (Y.Z.); +86-15882017032 (J.L.)

Abstract

Climate-driven extreme rainfall is increasing landslide risk, whereas conventional regional rainfall thresholds inadequately represent spatial variations in slope preconditioning across complex mountainous terrain. This study develops a dynamic early-warning framework that couples slope unit landslide susceptibility with rainfall triggering for Jinyang County, Southwest China. The county was divided into 7249 slope units, and eight conditioning factors were used to train support vector machine (SVM) and extreme gradient boosting (XGBoost) models with Bayesian hyperparameter optimization. Bayesian-optimized XGBoost (BO-XGBoost) achieved the best discrimination, with an area under the curve (AUC) of 0.893. For temporal triggering, 113 historical rainfall-landslide events were analyzed in logarithmic intensity–duration (I–D) space. A power-law fit described the central trend, and the fifth percentile of residuals defined a 5% non-exceedance threshold exceeded by approximately 95% of triggering events. Residual-based thresholds were used to establish four rainfall-trigger levels. A gated risk matrix coupled these levels with susceptibility classes. Validation using 162 online monitoring sites during the 21 August 2023 extreme rainfall event yielded 85.2% accuracy, 83.6% precision, 81.2% recall, 88.2% specificity, and an F1 score of 82.4%, demonstrating practical potential for spatially refined regional landslide early warning.

Keywords: slope unit; rainfall-induced landslide; susceptibility assessment; rainfall threshold; spatiotemporal early warning model

Academic Editors: Yiding Bao and Qiang Wei

Received: 27 July 2026
Revised: 4 September 2026
Accepted: 9 September 2026
Published: 13 September 2026

1. Introduction

China is among the countries most severely affected by geological hazards worldwide [1]. Rainfall-induced landslides represent a dominant geological hazard endangering lives and property across the country [2]. Accurate characterization of the spatiotemporal patterns of rainfall-induced landslides is critical for advancing regional landslide early warning performance and mitigating disaster risk [3]. The mountainous terrain of southwestern China features active tectonics and highly fragile hazard-preconditioning environments [4]. Passive evacuation measures, implemented solely in response to orange and red rainfall warnings issued by meteorological authorities [5], neglect the site-specific geological conditions of individual slopes. Such approaches suffer from low warning precision, imposing substantial implementation difficulties and uncertainty on local disaster prevention and mitigation efforts. Current work must address the limitations of standalone rainfall threshold models. Spatiotemporal early warning frameworks integrating landslide susceptibility (spatial probability) and critical rainfall thresholds (temporal probability) are required. Resolving variations in rainfall-hydrological responses across distinct geological preconditions and susceptibility grades enables the development of scientifically rigorous, precise, and spatially targeted landslide early warning methodologies, improving the accuracy and reliability of regional landslide warning systems.

Research on regional rainfall-induced landslide early warning has evolved from single-threshold analysis rooted in physical processes and empirical statistics to data-driven frameworks and multi-source information fusion [6]. Early work defined regional critical rainfall conditions via statistical links between rainfall intensity, duration, and landslide occurrence. Using 1951–2006 rainfall and landslide records, Dahal et al. [7] derived normalized thresholds for the Nepalese Himalayas, providing an empirical basis for regional rainfall-induced landslide warning. The accumulation of high-spatiotemporal-resolution meteorological data has redirected research focus from threshold fitting to warning performance optimization. Sala et al. [8] combined historical rainfall data with corrected weather radar observations and applied cost curves to assess missed and false alarm risks across threshold scenarios, delivering operational landslide early warning for Lombardy, Italy. Machine learning has further extended the representational capacity of landslide early warning systems. Rademann et al. [9] compared random forest, artificial neural network, and scoring table models, integrating geomorphic thresholds and rainfall data to underpin landslide susceptibility assessment and dynamic early warning in southern Brazil. Domestic studies have similarly moved beyond standalone rainfall thresholds toward integrated analysis of spatial susceptibility and temporal triggering conditions. Liu et al. [10] developed a regional landslide early warning model for Fujian Province using the random forest algorithm. Song et al. [11] proposed the PLEWM model, which couples landslide susceptibility and rainfall thresholds within a Bayesian framework, yielding substantially improved warning performance relative to conventional threshold models. Collectively, these findings demonstrate that integrating spatial landslide susceptibility with the temporal probability of rainfall triggering represents a key direction for advancing regional warning accuracy.

The reliability of landslide early warning models depends not only on rainfall metrics and modeling approaches but also on the delineation of spatial assessment units [12]. Grid units facilitate data processing but fragment natural geomorphic configurations. Catchment units support hydrological analysis but exhibit pronounced spatial scale heterogeneity [13]. Slope units, bounded by natural watershed divides and valley lines, retain intact natural slope morphology and spatial consistency of hazard-preconditioning factors including topography, lithology, and geological structure [14]. Adopting slope units as the basic assessment unit, integrated with coupled landslide susceptibility and critical rainfall thresholds, provides a physically meaningful spatial framework for refined, dynamic landslide early warning in complex mountainous regions.

This study was conducted in Jinyang County, Sichuan Province, Southwest China. Regional geological conditions, environmental factors, rainfall records, and historical landslide data were compiled to establish the research database. A total of 7249 slope units were delineated through DEM-based hydrological analysis and manual refinement, and eight conditioning factors, including engineering geological rock groups and slope structure, were aggregated at the slope unit scale. Bayesian optimization was employed to tune the hyperparameters of the SVM and XGBoost models, which were used to characterize spatial variations in landslide susceptibility. For temporal triggering analysis, the average rainfall intensity and duration of 113 historical rainfall–landslide events were projected onto a double-logarithmic I–D space. A power-law regression was first used to describe the central tendency of the samples, after which a 5% non-exceedance empirical threshold was derived from the fifth percentile of the residual distribution. Residual-based non-exceedance curves were further used to define blue, yellow, orange, and red rainfall-trigger levels. A gated risk matrix was then constructed to integrate static susceptibility grades with dynamic rainfall-trigger levels and update warnings for individual slope units. Event-based validation was conducted for the 21 August 2023 extreme rainfall event using 162 online monitoring sites with clearly identified deformation status. The results provide a practical basis for refined and dynamic landslide early warning in Jinyang County and other mountainous regions with comparable geological and geomorphic conditions.

2. Study Area and Data

2.1. Study Area Overview

2.1.1. Geographical Location

Jinyang County lies in southern Sichuan Province and eastern Liangshan Prefecture, within the transition zone from the Liangshan mountain plateau to the southwestern mountainous region [15]. Terrain across the county is generally higher in the west and lower in the east, with elevations spanning 460–4076 m. The Jinsha River and its tributaries (Xixi River, Jinyang River) deeply incise the land surface, creating canyons with 1000–3000 m vertical relief and a geomorphic pattern of alternating tectonically eroded alpine canyons, mid-alpine canyons, and low-mountain hilly platforms. Complex terrain and deeply incised valleys modulate regional rainfall-runoff convergence processes and shape the spatial distribution pattern of geological hazards, including landslides (Figure 1).

2.1.2. Regional Geological Setting

Jinyang County lies in the Xichang–Liangshan Uplift-Fold Zone of the Yangtze Paraplatform, adjacent to the Liangshan–Xiaojiang Fault Zone and affected by collision between the Indian and Eurasian plates (Figure 2). The county has undergone multiple episodes of subsidence, uplift, folding, and faulting, with three structural sets oriented northeast, north–south, and northwest, among which northeast-trending faults are most prominent. Intense tectonic activity along the Jinsha River and in the upper reaches of the Jinyang River produces fragmented rock masses with poor integrity, conditions conducive to the initiation and occurrence of geological hazards including landslides and rockfalls.

2.1.3. Meteorology and Hydrology

Jinyang County features a central subtropical monsoon climate with distinct dry and wet seasons, a mean annual temperature of 15.7 °C, and a mean annual precipitation of approximately 788.1 mm (Figure 3). Precipitation is seasonally concentrated, with wet-season rainfall reaching 700.8 mm, or 88.9% of the annual total. Such concentrated rainfall is the primary trigger for regional landslides.

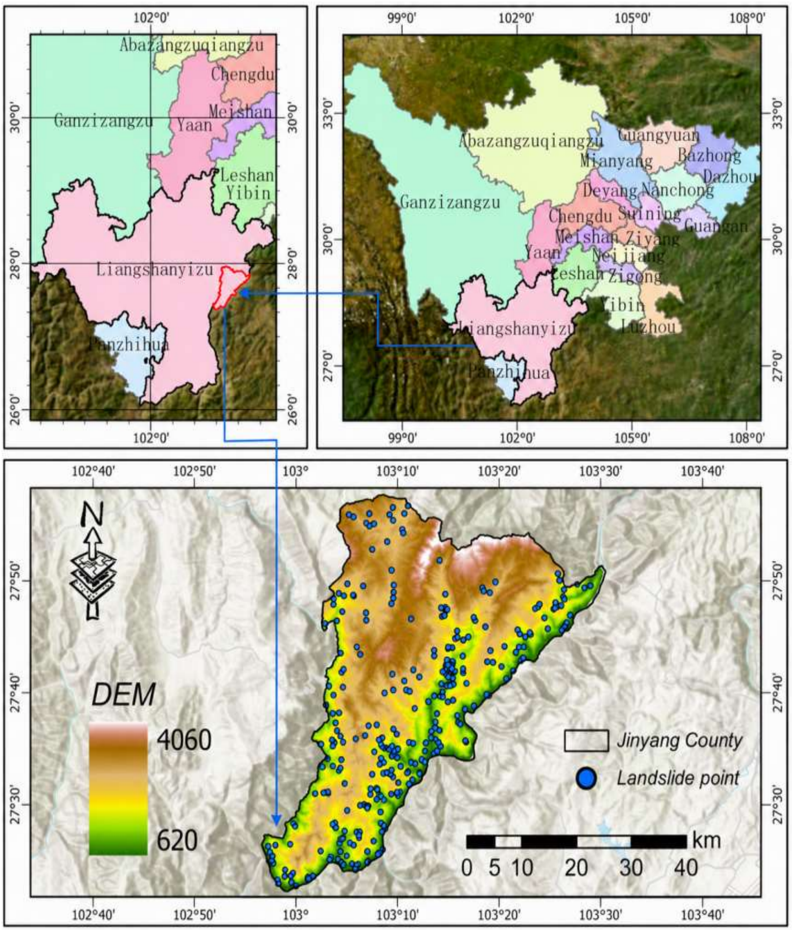

Figure 1. Geographical location and landslide distribution in Jinyang County.

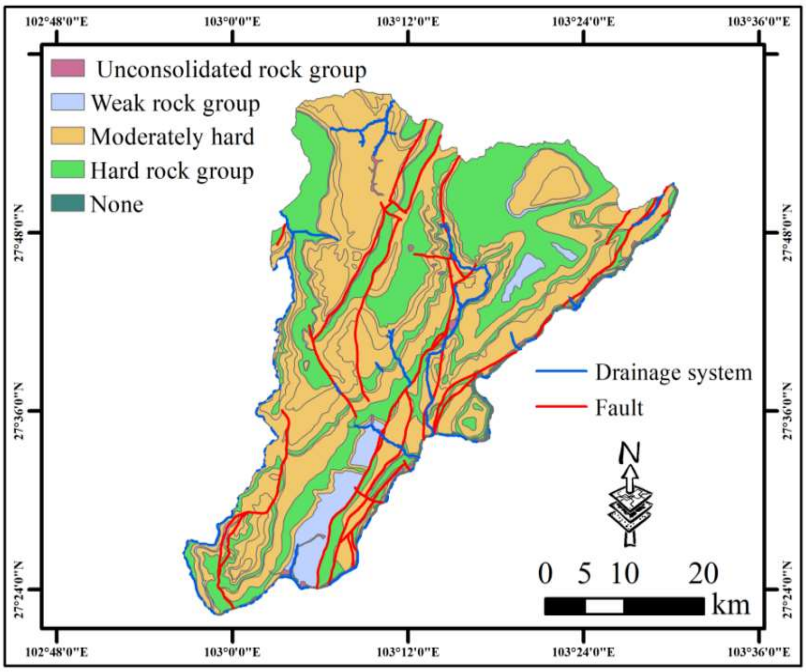

Figure 2. Distribution of geological conditions in Jinyang County.

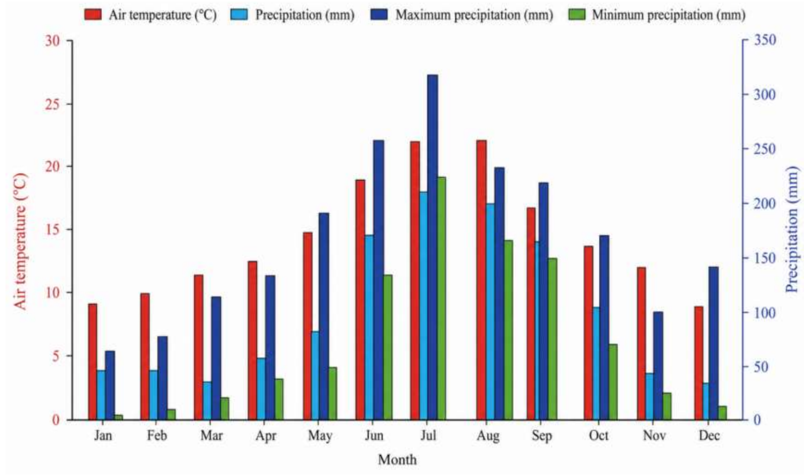

Figure 3. Meteorological data for Jinyang County.

2.2. Data Sources and Processing

2.2.1. Landslide Inventory

Landslide data are sourced from registered and historical hazard sites in the Jinyang County Geological Hazard Prevention Information Platform, together with remote sensing interpretation and field survey outputs from the project Detailed Investigation of Slope Geological Hazard Risks and Refined Survey of Key Townships in Jinyang County. Field verification yields 363 landslide sites, forming a landslide inventory for subsequent susceptibility modeling and analysis.

2.2.2. Basic Data Sources

All evaluation factors—integrating topography, geomorphology, geological structure, hydrology, and anthropogenic engineering activities across the study area—were aligned to a common coordinate system, clipped, topologically corrected, and resampled to a uniform spatial resolution. Zonal statistics were computed per slope unit. Continuous variables (slope gradient, NDVI, and distance-related factors) were assigned the area-weighted mean of valid pixels within each unit. Categorical variables, including engineering geological rock groups and slope structure, were assigned the dominant class by areal proportion. Aspect was reclassified into flat terrain and eight directional classes, with the majority class per unit retained. The result is a landslide susceptibility factor dataset organized by slope unit (data sources in Table 1).

Table 1. Sources of the basic data.

Data Type	Resolution	Source
Elevation	30 m	Geospatial Data Cloud https://www.gscloud.cn/ (accessed on 3 September 2026)
Lithology and structure	1:250,000	National Geological Archives of China https://www.ngac.cn/ (accessed on 3 September 2026)
Normalized Difference Vegetation Index (NDVI)	30 m	Derived from Landsat imagery via Google Earth Engine (GEE) https://code.earthengine.google.com (accessed on 3 September 2026)
Drainage network	/	Open Street Map https://www.openstreetmap.org/ (accessed on 3 September 2026)
Precipitation	/	Jinyang County Meteorological Bureau

3. Materials and Methods

3.1. Slope Unit Delineation and Factor Extraction

3.1.1. Slope Unit Delineation

Slope units are adopted as the basic units for landslide susceptibility assessment. Based on original and inverted DEMs, hydrological analysis is performed to compute sink filling, flow direction and flow accumulation, followed by extraction of drainage networks, ridge lines and valley lines. Initial slope units are generated by superimposing forward and reverse catchments [16]. Local unreasonable boundaries are manually verified and corrected with multi-temporal remote sensing imagery. A total of 7249 slope units are finally delineated across Jinyang County (Figure 4).

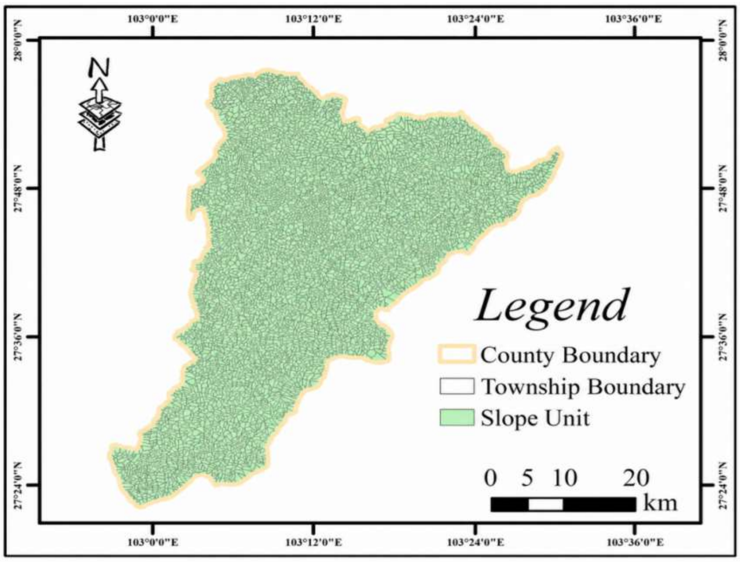

Figure 4. Slope unit delineation results.

3.1.2. Evaluation Factor Analysis

Landslide development is jointly controlled by topography, tectonic activity and human engineering activities [17]. Based on field surveys of the geological setting in Jinyang County, ten evaluation factors are initially selected with consideration of topographic relief, gully incision and lithological variation: NDVI, relief amplitude, distance to roads, distance to faults, distance to drainage networks, slope gradient, slope aspect, stratum lithology, terrain roughness and slope structure. Correlation analysis (Figure 5) reveals weak correlations ($|r| < 0.6$) among most factors except topographic metrics. A strong correlation is observed among slope gradient, terrain roughness, and relief amplitude.

In the alpine canyon terrain of Jinyang County, slope gradient exerts critical control over slope stress redistribution and landslide instability and is retained for evaluation. Eight factors are ultimately selected: NDVI, engineering geological rock groups, distance to roads, distance to faults, distance to drainage networks, slope gradient, slope aspect, and slope structure, forming a landslide susceptibility dataset with slope units as the basic evaluation units (Figure 6).

3.2. Landslide Susceptibility Model Construction

To quantify landslide occurrence probability across slope units, support vector machines, extreme gradient boosting, and their Bayesian-optimized variants are developed. Model discriminative performance is evaluated via receiver operating characteristic (ROC) curves and the corresponding area under the curve [18].

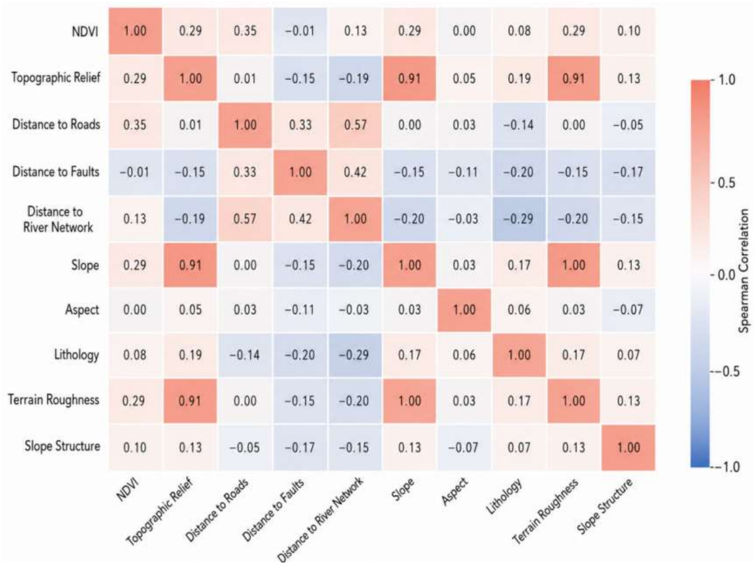

Figure 5. Correlation coefficient matrix of the landslide susceptibility conditioning factors.

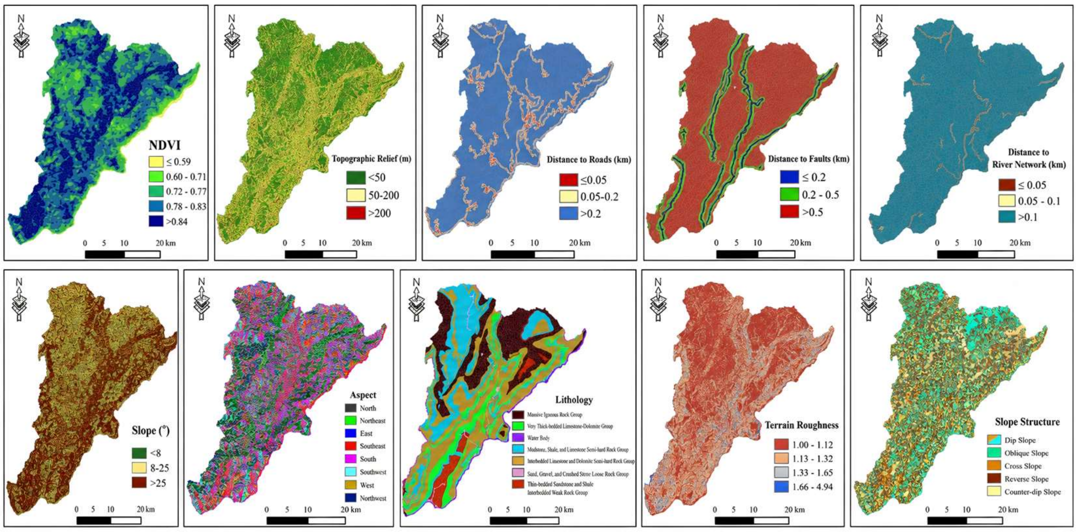

Figure 6. Spatial distributions of the conditioning factors.

3.2.1. Support Vector Machine

The support vector machine (SVM) is a supervised learning algorithm for nonlinear binary classification [19]. By mapping original features to a high-dimensional space via kernel functions, this method constructs an optimal classification hyperplane that maximizes the margin between landslide and non-landslide samples for effective binary discrimination. With robust nonlinear representational capacity and generalization performance, SVM is applicable to multi-factor landslide susceptibility assessment.

3.2.2. Extreme Gradient Boosting (XGBoost)

XGBoost is an ensemble learning algorithm built on gradient-boosted decision trees [20]. By iteratively introducing new decision trees to fit prediction residuals from the previous round, the model optimizes along the negative gradient direction of the loss function and integrates multiple weak learners into a high-performance classifier. Its objective function is formulated as:

$$Obj = \sum_{i=1}^{m} l(y_i, \hat{y}_i) + \sum_{k=1}^{K} \Omega(f_k) \tag{1}$$

where $l(\cdot)$ denotes the loss function, and $\Omega(\cdot)$ measures and regularizes tree model complexity to enhance generalization.

3.2.3. Bayesian Optimization

Predictive performance of machine learning models is highly sensitive to hyperparameter configurations. Complex high-dimensional nonlinear relationships prevail between landslide evaluation factors and landslide occurrence probability. Conventional grid search and random search require extensive model evaluations and fail to balance search efficiency with global optimization capacity. Bayesian optimization is adopted to automatically tune key hyperparameters of the SVM and XGBoost models.

Bayesian optimization takes model validation performance as its objective function. It approximates the hyperparameter–performance mapping via a probabilistic surrogate model and balances global exploration and local exploitation through an acquisition function [21]. Its core formulation is expressed as follows:

$$p(f|D_{1:t}) = \frac{p(D_{1:t}|f)p(f)}{p(D)} \tag{2}$$

The Bayesian optimization algorithm infers the distribution characteristics of the objective function from historical optimization results (posterior information) and iteratively selects the most promising observation points to yield its global optimum.

3.2.4. Sample Collection

A spatially explicit sample database underpins the predictive performance and generalization of machine learning models. Delineated slope units served as the basic units for sample selection, attribute extraction, and class assignment. Bounded naturally by drainage divides and valley lines, these units were generated through hydrological analysis of a DEM and its inverse, with locally inconsistent boundaries manually refined against remote sensing imagery. The delineation preserves hillslope topology, geomorphic form, and hydrological boundary characteristics. A binary landslide susceptibility sample database was then constructed from the landslide inventory [22].

Slope units containing landslide points were defined as positive samples and labeled 1; multiple landslide points within the same unit were merged into one sample(Figure 7). To mitigate label bias introduced by spatial clustering and incomplete inventory, a 1 km exclusion buffer was established around each landslide point. This distance serves only to filter candidate negative samples and does not represent the extent of landslide influence. Units outside the buffer, containing no known landslides and verified as relatively stable, were selected as negative samples and labeled 0, with duplicate units removed. The dataset was stratified into training and test sets at a 7:3 ratio, and five-fold cross-validation was applied to the training set for model training and hyperparameter optimization [23].

3.2.5. Hyperparameter Optimization

Bayesian optimization is employed to tune key hyperparameters of SVM and XGBoost, with a maximum of 100 iterations. The optimized parameter combinations and initial baseline model settings are listed in Table 2. The resulting configurations for BO-SVM and BO-XGBoost align with the study area's complex environmental features, supporting subsequent model performance comparison.

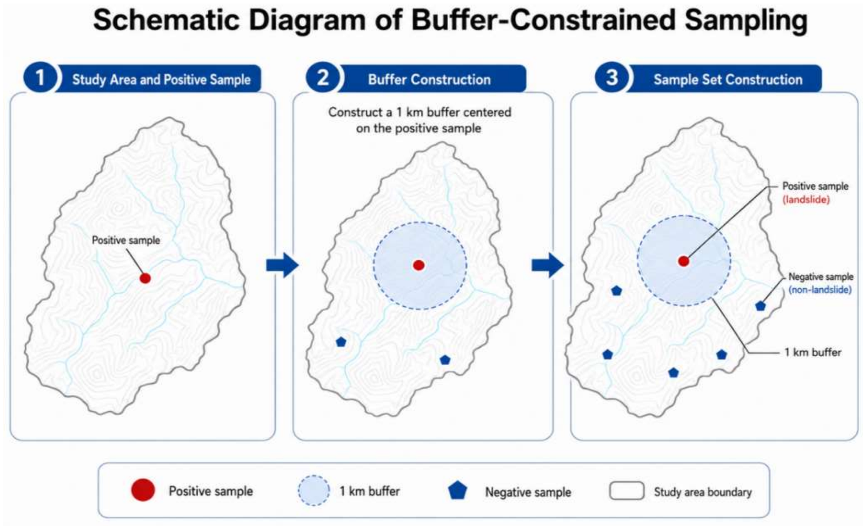

Figure 7. Sampling scheme.

Table 2. Optimized hyperparameter combinations for the models.

Model	C	Gamma	Learning_Rate	Max_Depth	N_Estimators
SVM	1	scale	/	/	/
BO-SVM	2.48	0.176	/	/	/
XGBoost	/	/	0.30	6	100
BO-XGBoost	/	/	0.06	10	75

3.3. I–D Rainfall Threshold Model

To characterize rainfall controls on landslide occurrence and develop a site-specific rainfall early-warning model for Jinyang County, hourly rainfall data and records of landslide disasters and hazardous events within and around the county were compiled (Figure 8).

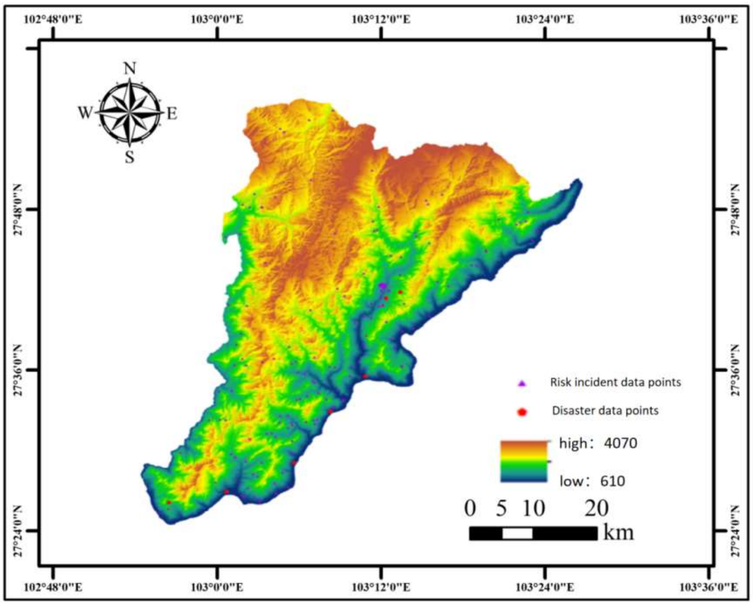

Figure 8. Spatial distribution of landslide disasters and hazardous events in Jinyang County.

3.3.1. Rainfall Event Extraction and Data Processing

Multi-year rainfall patterns in Jinyang County are analyzed. A threshold of $\leq$5 mm cumulative rainfall over 6 consecutive hours is adopted to delineate individual rainfall events and standardize their onset and end times [24]. Raw samples are filtered to exclude outliers with mismatched rainfall processes or pronounced anomalous rainfall features. Rainfall processes are matched to the occurrence times of 172 landslide disaster and hazard events. Characteristic parameters including mean rainfall intensity (I), rainfall duration (D) and cumulative rainfall (E) are derived. A total of 113 valid rainfall-landslide events are retained as source data for I–D threshold model fitting (Table 3).

3.3.2. I–D Threshold Model Construction

Critical rainfall thresholds for geological hazards are commonly determined by single-line, double-line, or triple-line methods, of which the single-line method is most widely applied [25]. We adopt the rainfall intensity–duration (I–D) single-line model, projecting the mean rainfall intensity I and rainfall duration D of 113 landslide-triggering rainfall events onto log–log coordinates. The central trend of the sample is fitted by power-law regression, and a 5% non-exceedance-probability empirical threshold curve is constructed from the 5th percentile of the empirical distribution of the fitting residuals. The curve is exceeded by approximately 95% of historical landslide-triggering events and delineates the empirical lower bound of mean rainfall intensity for different rainfall durations under the existing triggering samples. Because complete non-triggering rainfall events have not yet been incorporated, the curve does not represent the optimal boundary between triggering and non-triggering events, nor does it denote the absolute minimum mean rainfall intensity required to induce geological hazards. The general form of the I–D empirical threshold is:

$$\mathrm{I} = \mathrm{CD}^{-\alpha} \tag{3}$$

where I is the mean rainfall intensity (mm h^{-1}), D is the rainfall duration (h), and C and α are regional empirical constants.

3.3.3. Graded Early-Warning Thresholds

Following the Specification for Automatic Monitoring and Early Warning of Geological Hazards (DZ/T 0460—2023), meteorological risk warnings are classified into four grades: IV (blue), III (yellow), II (orange), and I (red). To avoid the subjectivity of shifting threshold curves by fixed ratios, we fitted the central-trend relationship between mean rainfall intensity I and rainfall duration D for 113 historical landslide-triggering rainfall events in log–log space, and constructed graded non-exceedance-probability thresholds from the empirical cumulative distribution of the fitting residuals [26]. The thresholds T_5, T_{20}, T_{50}, and T_{80} correspond to the 5th, 20th, 50th, and 80th percentiles of the residual distribution: no warning below T_5; grade IV (blue) from T_5 to T_{20}; grade III (yellow) from T_{20} to T_{50}; grade II (orange) from T_{50} to T_{80}; and grade I (red) at or above T_{80}. These non-exceedance proportions give the cumulative proportion of historical landslide-triggering events lying below the corresponding threshold curve; they characterize the relative grade of rainfall-triggering conditions and do not represent landslide probability.

3.4. Coupled Susceptibility–Rainfall Trigger Early-Warning Model

To couple spatial susceptibility and temporal triggering of rainfall-induced landslides, slope units serve as the minimum warning units. Susceptibility grades are taken as spatial priors, and real-time I–D threshold discrimination results are used as dynamic triggers. Integrated judgment is performed via a gated risk matrix superposition approach [27], formulated as:

$$W_i(t) = M(S_i, R_i(t)) = M(S_i, R(I_i(t), D_i(t))) \tag{4}$$

where R(·) is the rainfall trigger discrimination operator based on graded I–D thresholds, and M(·) is the gated risk matrix mapping operator.

Table 3. Relationship between rainfall and landslide disaster and hazard events in Jinyang County.

Disaster Number	Occurrence Date	Occurrence Time	I/(mm h^{-1})	D/h	E/mm	Disaster Number	Occurrence Date	Occurrence Time	I/(mm h^{-1})	D/h	E/mm
Z1	11 May 2022	12:00	9.22	6.0	55.33	Z58	29 August 2008	6:22	22.90	2.0	45.80
Z2	22 September 2023	22:10	7.23	7.0	50.61	Z59	12 August 2014	17:11	2.40	30.0	72.00
Z3	9 February 2023	10:00	4.06	8.0	32.47	Z60	7 July 2017	14:38	2.40	8.0	19.20
Z4	16 September 2023	16:30	2.71	14.0	38.01	Z61	1 August 1993	0:30	20.94	1.0	20.94
Z5	15 September 2023	15:40	0.80	48.0	38.24	Z62	1 November 2020	22:21	26.32	2.0	52.65
Z6	16 January 2024	9:00	8.08	4.0	32.31	Z63	14 September 2023	22:06	2.00	22.0	44.00
Z7	5 January 2024	17:04	1.62	32.0	51.95	Z64	28 August 2014	2:20	1.90	49.0	93.10
Z8	5 February 2024	20:38	6.62	5.0	33.08	Z65	2 July 1998	12:58	4.10	5.0	20.50
Z9	14 June 2009	17:50	0.91	30.0	27.20	Z66	28 August 2013	17:35	2.60	10.0	26.00
Z10	5 July 2008	20:42	8.73	3.0	26.18	Z67	3 April 1990	12:04	20.08	1.0	20.08
Z11	9 May 2010	22:34	7.21	4.0	28.84	Z68	21 September 2000	20:35	10.90	3.0	32.69
Z12	13 August 2004	4:25	2.08	20.0	41.56	Z69	15 September 2013	4:20	15.35	1.0	15.35
Z13	18 June 2008	12:54	7.92	5.0	39.60	Z70	27 October 2008	12:59	9.94	3.0	29.81
Z14	4 March 2007	6:05	8.60	4.0	34.41	Z71	7 January 1995	23:45	49.74	1.0	49.74
Z15	20 January 2008	5:28	5.17	4.0	20.66	Z72	17 February 2008	7:12	26.18	2.0	52.36
Z16	14 September 2011	7:23	9.81	6.0	58.85	Z73	1 February 2012	14:56	31.68	1.0	31.68
Z17	17 June 2012	3:58	10.25	5.0	51.27	Z74	19 September 2019	20:54	0.40	82.0	32.80
Z18	17 September 2015	9:13	0.79	22.0	17.28	Z75	19 September 2019	1:57	17.52	1.0	17.52
Z19	19 July 2015	12:34	3.78	9.0	34.03	Z76	14 December 2016	20:08	16.30	4.0	65.20
Z20	17 May 2014	17:47	4.72	7.0	33.01	Z77	19 December 2017	23:37	2.70	11.0	29.70
Z21	12 July 2007	10:38	4.81	11.0	52.94	Z78	16 March 2023	17:42	23.70	1.0	23.70
Z22	7 August 2007	4:11	9.34	5.0	46.68	Z79	16 March 2020	18:43	3.10	9.0	27.90
Z23	10 March 2013	4:29	1.84	18.0	33.21	Z80	1 July 2010	16:25	5.30	8.0	42.40
Z24	27 February 2014	1:53	7.40	8.0	59.21	Z81	4 November 2013	6:00	10.88	3.0	32.64
Z25	21 August 2014	17:15	10.31	5.0	51.54	Z82	23 February 2011	6:49	46.89	1.0	46.89
Z26	4 April 2014	14:11	3.70	16.0	59.21	Z83	8 January 2011	13:03	19.76	3.0	59.27
Z27	3 May 2015	0:46	9.20	5.0	46.02	Z84	4 July 2017	2:12	0.60	39.0	23.40
Z28	11 July 2003	17:52	0.89	34.0	30.36	Z85	5 May 2018	4:02	11.22	5.0	56.12
Z29	13 September 1983	14:15	4.68	12.0	56.14	Z86	4 December 2018	13:07	24.61	2.0	49.22
Z30	17 September 2013	13:50	10.41	4.0	41.66	Z87	17 September 2013	15:48	0.90	66.0	59.40
Z31	25 August 2010	11:08	5.41	3.0	16.22	Z88	5 May 2018	11:17	2.20	45.0	99.00
Z32	13 April 2015	17:49	1.81	14.0	25.40	Z89	9 August 2014	23:30	12.16	6.0	72.95
Z33	30 April 2017	17:13	0.40	76.0	30.34	Z90	25 April 2015	7:30	3.27	21.0	68.67
Z34	28 February 2017	16:13	1.19	33.0	39.35	Z91	4 July 2012	17:30	8.73	8.0	69.85
Z35	1 July 2018	5:53	6.05	3.0	18.15	Z92	27 July 1995	21:40	3.23	22.0	70.97

Table 3. *Cont.*

Disaster Number	Occurrence Date	Occurrence Time	I/(mm h^{-1})	D/h	E/mm	Disaster Number	Occurrence Date	Occurrence Time	I/(mm h^{-1})	D/h	E/mm
Z36	1 August 2017	18:59	4.13	10.0	41.34	Z93	18 September 2015	21:30	4.97	17.0	84.53
Z37	20 August 2018	8:22	1.36	27.0	36.74	Z94	6 August 2014	22:20	1.34	31.0	41.41
Z38	17 May 2015	14:18	2.86	13.0	37.16	Z95	30 April 2017	10:00	8.45	11.0	92.97
Z39	3 August 2015	15:31	5.44	4.0	21.76	Z96	1 August 2017	10:00	12.02	4.0	48.09
Z40	26 April 2003	20:55	3.20	7.0	22.40	Z97	11 September 2023	10:00	1.74	20.0	34.73
Z41	15 September 2012	14:11	5.10	6.0	30.60	Z98	7 September 2023	0:15	2.10	25.0	52.60
Z42	20 January 1960	22:09	11.50	4.0	46.00	Z99	10 August 2009	0:20	2.22	27.0	59.97
Z43	14 May 1960	15:49	18.86	2.0	37.71	Z100	16 June 1998	0:20	3.21	18.0	57.87
Z44	14 April 2015	2:54	24.36	1.0	24.36	Z101	1 March 2014	1:15	5.61	11.0	61.74
Z45	14 May 2008	6:08	6.10	8.0	48.80	Z102	19 March 2014	0:40	21.11	3.0	63.33
Z46	1 June 2013	18:33	3.50	17.0	59.50	Z103	14 May 2014	17:30	10.11	4.0	40.43
Z47	12 December 2017	7:24	22.87	1.0	22.87	Z104	25 January 2014	17:30	1.76	58.0	102.31
Z48	17 December 2019	22:50	4.90	6.0	29.40	Z105	5 July 2017	22:30	4.18	16.0	66.86
Z49	27 September 2023	21:51	2.10	22.0	46.20	Z106	26 May 2013	22:30	32.06	3.0	96.18
Z50	18 April 2019	16:20	1.80	40.0	72.00	Z107	4 August 2014	13:10	7.33	7.0	51.31
Z51	17 August 2013	13:27	39.28	1.0	39.28	Z108	7 August 2014	17:30	4.30	10.0	43.05
Z52	11 August 2014	4:59	1.10	48.0	52.80	Z109	7 August 2014	20:50	0.66	70.0	46.31
Z53	24 August 2014	12:54	3.30	15.0	49.50	Z110	27 August 2015	16:10	19.63	4.0	78.51
Z54	1 August 2004	5:47	24.33	2.0	48.66	Z111	17 September 2015	2:00	3.44	16.0	55.12
Z55	11 June 2014	17:19	14.20	3.0	42.60	Z112	28 June 2021	21:00	10.43	6.0	62.58
Z56	12 August 2010	9:43	13.38	4.0	53.53	Z113	18 August 2021	7:30	19.30	2.0	38.61
Z57	8 July 2013	18:27	17.84	3.0	53.52						

Note: I = rainfall intensity; D = rainfall duration; E = cumulative rainfall.

The warning remains inactive when rainfall fails to reach the minimum trigger threshold. Once triggered, final warning levels are determined by combinations of rainfall grade and landslide susceptibility grade. The model maps real-time rainfall dynamics to slope units at hourly resolution, with results aggregated to administrative units such as townships, yielding regional warnings with spatial differentiation and temporal dynamic updating.

4. Results

4.1. Accuracy Comparison of Landslide Susceptibility Models

Model performance is evaluated using accuracy, precision, recall, F1-score, and AUC (Table 4). Bayesian optimization yields performance improvements across all models, with BO-XGBoost outperforming baseline counterparts on every metric.

Table 4. Accuracy statistics for the landslide susceptibility models.

Model	Accuracy	Precision	Recall	F1	AUC
SVM	0.769	0.729	0.732	0.730	0.790
BO-SVM	0.809	0.775	0.783	0.779	0.883
XGBoost	0.776	0.730	0.757	0.744	0.842
BO-XGBoost	0.817	0.787	0.787	0.787	0.893

SVM, BO-SVM, XGBoost, and BO-XGBoost achieve AUC values of 0.790, 0.883, 0.842, and 0.893, respectively (Figure 9). With the highest AUC, BO-XGBoost exhibits the strongest discriminative and generalization performance.

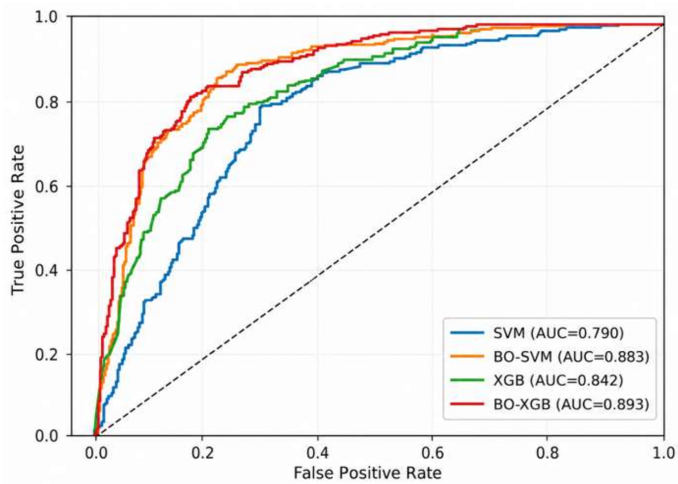

Figure 9. Receiver operating characteristic curves for the four susceptibility models.

4.2. Rainfall-Induced Landslide Susceptibility Results

Slope unit landslide susceptibility results derived from the SVM, XGBoost, BO-SVM and BO-XGBoost models are classified into grades via the natural breaks method to generate susceptibility zonation maps (Figure 10). All model outputs align broadly with the spatial distribution of historical landslide sites. Moderate and high susceptibility zones occur as linear belts along the Jinsha, Xixi, and Jinyang rivers, governed by fluvial dissection, tectonic fragmentation, intense rainfall, and engineering disturbance; localized high-susceptibility patches in Tiandiba and Lugao towns exhibit a scattered pattern, linked to steep terrain, reduced rock–soil mass stability, and human activities, including slope cutting for construction and mining operations. Low and very low susceptibility zones cluster in the county's northeastern and northwestern regions, with gentle topography, relatively stable tectonic settings and limited anthropogenic activity underpinning high overall slope stability.

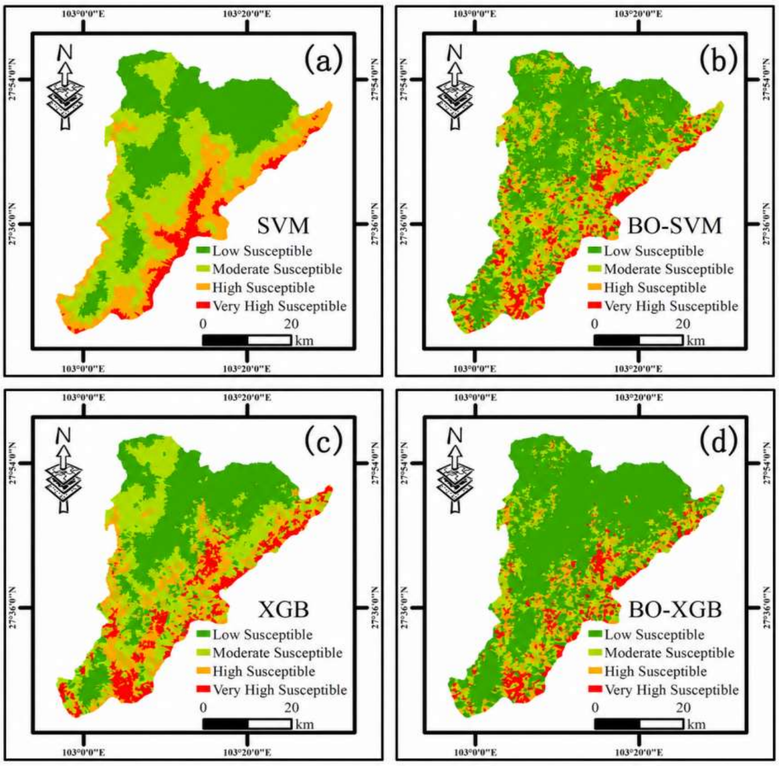

Figure 10. Landslide susceptibility zoning maps generated by the four models. ((**a**) SVM model susceptibility partition map, (**b**) BO-svm model susceptibility partition map, (**c**) XGB model susceptibility partition map, (**d**) BO-XGB model susceptibility partition map).

4.3. Rainfall Thresholds and Graded Early-Warning Results

4.3.1. Rainfall Threshold Analysis

The mean rainfall intensity (I) and rainfall duration (D) of the 113 landslide-triggering rainfall events in the study area were projected onto a double-logarithmic coordinate system. A power-law regression was first applied to capture the central trend of the dataset. From the 5th percentile of the empirical distribution of the fitting residuals, a 5% non-exceedance probability empirical I–D threshold curve was then constructed, which represents the lower rainfall limit exceeded by approximately 95% of the historical landslide-triggering events (Figure 11). $IT5 = 16.505D^{-0.880}$. This threshold acts as a probabilistic empirical lower bound from a statistical perspective, rather than the absolute minimum rainfall requirement for landslide occurrence.

Critical rainfall conditions exhibit considerable regional variability and are jointly controlled by rainfall intensity and duration. Using 113 historical landslide-triggering rainfall events from the study area, this study constructs a 5% non-exceedance-probability empirical I–D threshold based on the 5th percentile derived from the empirical distribution of fitting residuals ($IT5 = 16.505D^{-0.880}$). Approximately 94.7% of the 113 triggering events lie above this curve. Empirical thresholds for mean rainfall intensity and cumulative rainfall corresponding to different rainfall durations were further calculated (Table 5). When observed rainfall meets or exceeds these thresholds, the prevailing rainfall conditions fall within the empirical lower-bound range of historical landslide-triggering events, implying an elevated probability of landslide occurrence. These thresholds can serve as rainfall criteria for triggering or strengthening monitoring and early-warning activities. Nevertheless, they neither guarantee landslide initiation nor define the absolute minimum hazard-inducing rainfall condition.

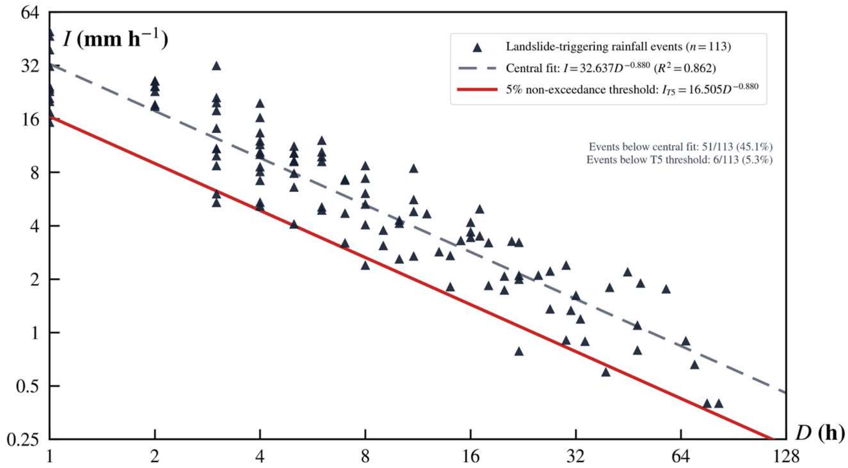

Figure 11. Fitted rainfall intensity–duration threshold.

Table 5. Rainfall thresholds for rainfall-induced landslides in Jinyang County.

D/h	I/(mm h^{-1})	E/mm	D/h	I/(mm h^{-1})	E/mm
1.0	16.51	16.51	13.0	1.73	22.43
2.0	8.97	17.93	14.0	1.62	22.63
3.0	6.27	18.82	15.0	1.52	22.82
4.0	4.87	19.48	16.0	1.44	22.99
5.0	4.00	20.01	17.0	1.36	23.16
6.0	3.41	20.45	18.0	1.30	23.32
7.0	2.98	20.83	19.0	1.24	23.47
8.0	2.65	21.17	20.0	1.18	23.62
9.0	2.39	21.47	21.0	1.13	23.75
10.0	2.17	21.74	22.0	1.09	23.89
11.0	2.00	21.99	23.0	1.04	24.01
12.0	1.85	22.22	24.0	1.01	24.14

4.3.2. Graded Early Warning

Based on the I–D relationship derived from 113 historical landslide-triggering rainfall events in the study area, this study calculated the empirical distribution of logarithmic residuals after fitting the central trend. Four sets of parallel threshold curves (blue, yellow, orange, and red) were constructed by adopting non-exceedance fractions of 5%, 20%, 50%, and 80%, respectively. Each non-exceedance fraction denotes the proportion of historical triggering events falling below the corresponding threshold curve, rather than the probability of landslide occurrence. Standard durations of 1, 3, 6, 12, 24, and 48 h were input into the graded model to obtain the corresponding critical mean rainfall intensity values (Table 6). On this basis, a multi-duration rainfall early-warning indicator system with step-by-step escalation from low to high levels was established (Figure 12).

Table 6. Critical rainfall-line equations for graded rainfall-induced landslide warning in Jinyang County.

Rainfall Parameter Index Type	Envelope Range, R	Critical Rainfall Line Equation
Red warning	$R \geq 80\%$	$I = 46.672D^{-0.880}$
Orange warning	$50\% \leq R < 80\%$	$I = 34.322D^{-0.880}$
Yellow warning	$30\% \leq R < 50\%$	$I = 23.174D^{-0.880}$
Blue warning	$R < 30\%$	$I = 16.505D^{-0.880}$

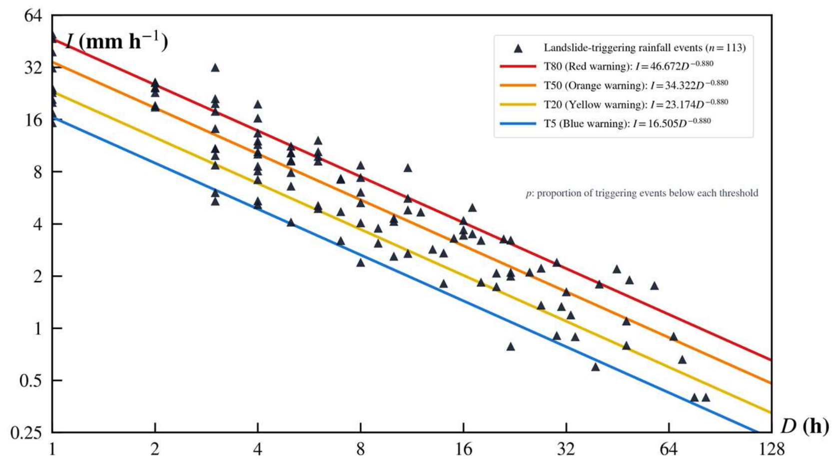

Figure 12. Graded rainfall threshold model for landslide early warning in Jinyang County.

4.3.3. Early-Warning Model Grading

To comprehensively characterize static landslide susceptibility and dynamic rainfall-triggering conditions, this study took landslide susceptibility classes derived from the BO-XGBoost model as the vertical axis. The horizontal axis represents the position of normalized real-time rainfall indicators relative to the T5, T20, T50 and T80 non-exceedance-probability threshold curves. A meteorological risk early-warning judgment matrix for rainfall-induced landslides in Jinyang County was established via gating coupling (Figure 13). No meteorological warning is issued for any susceptibility class when (Z < 16.505, Z = ID$^{0.880}$). As both the rainfall-triggering level and landslide susceptibility level increase, the integrated warning level escalates progressively from Level V (no warning) to Level I (alert). This matrix reflects the joint empirical classification of landslide susceptibility and historical hazard-causing rainfall conditions, and does not directly quantify landslide occurrence probability.

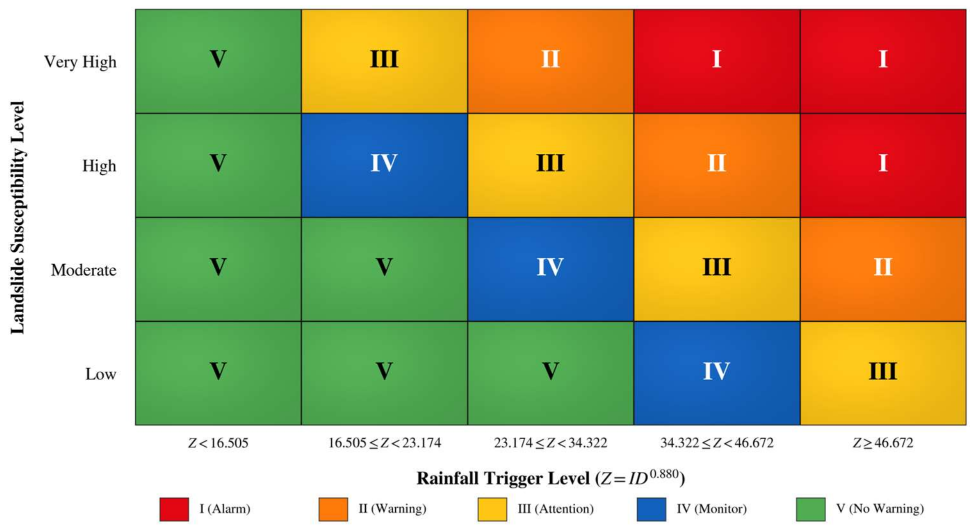

Figure 13. Gated risk matrix for graded landslide early warning.

4.4. Coupled Early-Warning Model Validation

The practical performance of the coupled early warning model was tested against the heavy rainfall event in Jinyang County on 21 August 2023. Rain gauge observations were spatially interpolated to derive the rainfall distribution across the study area, and the mean rainfall intensity and duration were mapped to 7249 slope units. Landslide susceptibility classes from the BO-XGBoost model and real-time I–D threshold discrimination were combined in a gated risk matrix to compute the warning level for each slope unit, yielding the landslide meteorological risk warning zoning map for the "8·21" rainfall event in Jinyang County (Figure 14).

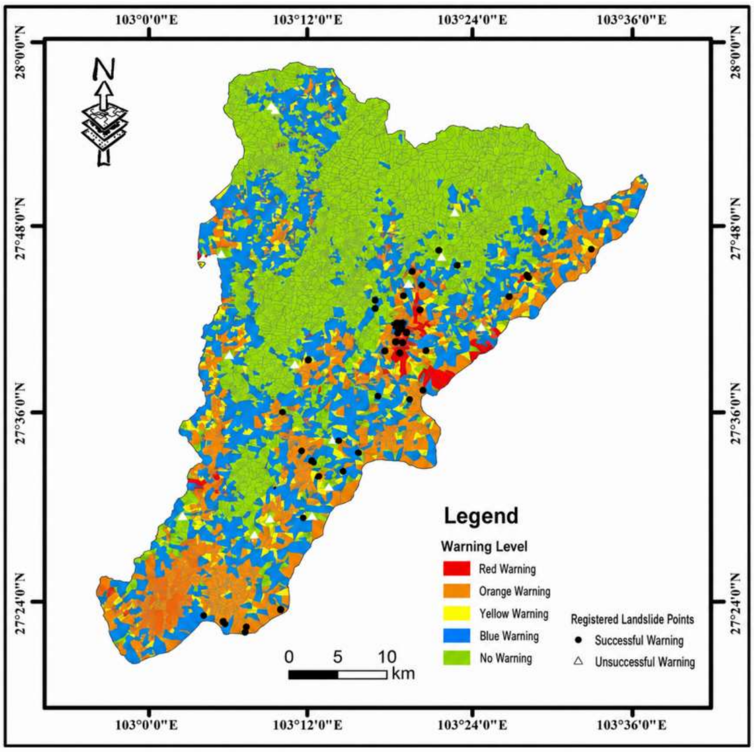

Figure 14. Landslide rainfall early-warning zoning for Jinyang County on 21 August 2023.

For validation, red, orange, yellow, and blue warning levels were merged as model-issued warnings, with green units treated as unwarned. Of the 162 operational monitoring points, 69 deformed during the rainfall event and 93 remained stable. Among the deforming points, 56 corresponding units were successfully warned and 13 were missed; among the stable points, 11 corresponding units generated false alarms, and 82 remained unwarned. These counts constitute a standard binary classification contingency matrix covering all operational monitoring points (Table 7; Figure 15).

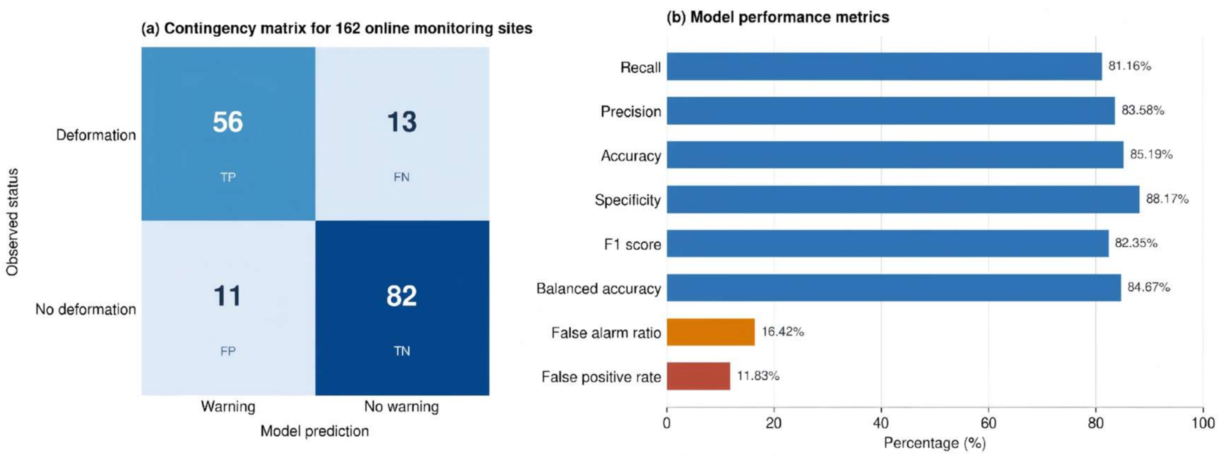

Figure 15. Validation results of the coupled early-warning model for the 21 August 2023 rainfall event in Jinyang County: (**a**) confusion matrix for 162 online monitoring points; (**b**) model performance metrics.

Table 7. Model validation contingency matrix for 162 online monitoring sites.

Observed Status	Warning Issued	No Warning	Total
Deformation	56 (TP)	13 (FN)	69
No deformation	11 (FP)	82 (TN)	93
Total	67	95	162

Ten performance metrics were computed from Table 7: overall accuracy, precision, recall, miss rate, false positive rate (FPR), specificity, false alarm ratio (FAR), F1 score, critical success index, and balanced accuracy. FAR uses all model-issued warnings as its denominator, representing the share of issued warnings with no deformation. FPR uses all actually non-deforming monitoring points as its denominator, reflecting the fraction of stable points falsely warned. Results are given in Table 8.

Table 8. Performance evaluation of the coupled early-warning model.

Model	Accuracy	Precision	Recall	MR	FPR	Specificity	FAR	F1-Score	CSI	Balanced Accuracy
Early-warning model	85.19%	83.58%	81.16%	18.84%	11.83%	88.17%	16.42%	82.35%	70.00%	84.67%

For the 162 operational monitoring points, model recall reached 81.16%, capturing most deforming points. Precision and F1 score were 83.58% and 82.35%, respectively, and overall accuracy was 85.19%. The false positive rate among non-deforming points was 11.83% (specificity, 88.17%); the false alarm ratio across all issued warnings was 16.42%. Within the monitored domain, the model balances deformation detection with false-alarm control, although 13 points were missed and 11 false alarms were recorded. The coupled model effectively characterizes the spatiotemporal risk of rainfall-induced landslides in complex mountainous terrain and provides technical support for regional landslide early warning and risk prevention and control.

5. Discussion

Focusing on the typical alpine canyon terrain of Jinyang County, this study developed a slope unit-based landslide susceptibility model using Bayesian-optimized extreme gradient boosting (BO-XGBoost) and coupled it with rainfall intensity–duration (I–D) thresholds to establish a spatiotemporal early-warning model. The following discussion addresses the applicability of slope-unit-scale warning, the significance of susceptibility–rainfall coupling, and model uncertainty.

5.1. Applicability of Slope-Unit-Scale Warning

The selection of assessment units directly determines the capacity of landslide susceptibility models to characterize geological environments. Jinyang County, an alpine canyon region with pronounced topographic relief and intense fluvial dissection by the Jinsha River drainage network, sees stronger applicability of slope units than grid and slope gradient units. Devoid of geomorphic boundaries, grid units tend to fragment slope continuity; slope gradient units, despite capturing topographic variability, fail to represent couplings among hillslope runoff convergence, rainfall infiltration, and geological conditions [28]. Bounded by drainage divides and gully lines, slope units carry clearer hydrogeomorphic significance and better capture hillslope hydrological responses and landslide preparation processes. The slope-unit-based BO-XGBoost model yields an AUC value of 0.893, indicating high discriminative performance and validating the suitability of slope units for landslide susceptibility assessment in complex alpine canyon terrain.

5.2. Significance of Coupling Landslide Susceptibility with Rainfall Thresholds

This study employs a gated risk matrix superposition method to integrate landslide susceptibility assessment with rainfall thresholds, enabling the transition from static susceptibility evaluation to dynamic early warning. Within this framework, susceptibility grades reflecting slope failure likelihood calibrate regional early-warning thresholds. High-susceptibility zones with diminished slope stability meet warning criteria under low rainfall magnitudes, whereas low-susceptibility zones require higher rainfall inputs [29]. Accounting for spatial heterogeneity in landslide occurrence, this approach produces early-warning outputs closely aligned with field conditions in Jinyang County.

5.3. Model Uncertainty and Future Improvements

Although the slope unit coupled early warning model delivered reasonable warning performance during the "8·21" event in Jinyang County, its applicability remains constrained by data availability. Both the susceptibility model and I–D thresholds were calibrated exclusively on Jinyang County data. Slope units capture spatial variations in lithology, topography, and hydrology, yet a single-region I–D relationship cannot fully resolve hydro-mechanical heterogeneity within the county or across regions. The current thresholds derive primarily from 113 landslide-triggering rainfall events; without complete non-triggering rainfall samples, optimal discrimination thresholds cannot be established via ROC analysis. Validation drew on 162 operational monitoring points from a single event, so the results are not directly generalizable to all 7249 slope units, and model robustness under extreme rainfall remains untested. Future work will compile multi-region, multi-event triggering and non-triggering rainfall records, incorporate antecedent rainfall, soil moisture, and geomechanical parameters to develop zoned I–D thresholds, and integrate satellite remote sensing, InSAR deformation monitoring, and independent event validation to enhance regional applicability and warning reliability.

6. Conclusions

Using slope units as the fundamental assessment units, we systematically examine the relationship between landslide susceptibility and rainfall conditions in Jinyang County, develop a county-specific rainfall early-warning model, and present the following conclusions.

(1) Slope units are widely adopted for geological hazard susceptibility assessment. Compared to conventional grid, slope gradient, and catchment units, those derived via hydrological analysis with manual refinement more accurately capture the spatial heterogeneity of in situ slope conditions and fundamental geological environmental factors.

(2) Among the four landslide susceptibility models built on slope units, the BO-XGBoost model (0.893) outperforms the other three, exhibiting superior applicability. High- and medium-susceptibility zones are concentrated along the Jinsha River, in Tiandiba Town, Lugao Town, and other areas with complex geological structures and dense populations. Low-susceptibility zones occur in the topographically gentle northeast and northwest. These results closely match the spatial distribution of historical landslide events in Jinyang County.

(3) The rainfall early-warning model coupling BO-XGBoost-derived landslide susceptibility grades with a rainfall intensity–duration (I–D) model is well suited to Jinyang County, with strong early-warning performance observed during the 21 August intense rainfall event. This model provides technical support for landslide hazard prevention and early warning in Jinyang County, effectively mitigating associated disaster losses.

Author Contributions: Conceptualization, J.Y. and Q.H.; methodology, F.Z., Y.Z., J.L. and Q.X.; software, F.Z.; validation, Q.X. and L.J.; formal analysis, S.S.; investigation, F.Z., J.L. and P.W.;

resources, J.L., Q.H. and P.W.; data curation, J.L.; writing—original draft preparation, F.Z.; writing—review and editing, Y.Z., Q.X. and L.J.; visualization, Y.Z., L.J. and S.S.; supervision, J.Y.; funding acquisition, J.Y. All authors have read and agreed to the published version of the manuscript.

Funding: This research was funded by the China Geological Survey, grant number DD202606101201.

Institutional Review Board Statement: Not applicable.

Informed Consent Statement: Not applicable.

Data Availability Statement: The data presented in this study are available on request from the corresponding authors.

Acknowledgments: We sincerely thank the Natural Resources Bureau of Jinyang County for providing all the information and related support.

Conflicts of Interest: Author Shilong Sun was employed by the company Sichuan Huadi Construction Engineering Co., Ltd. The remaining authors declare that the research was conducted in the absence of any commercial or financial relationships that could be construed as a potential conflict of interest.

References

1. Shu, B.; Chen, Y.; Amani-Beni, M.; Zhang, R. Spatial distribution and influencing factors of mountainous geological disasters in southwest China: A fine-scale multi-type assessment. *Front. Environ. Sci.* **2022**, *10*, 1049333. [CrossRef]
2. Nie, W.; Tian, C.; Song, D.; Liu, X.; Wang, E. Disaster process and multisource information monitoring and warning method for rainfall-triggered landslide: A case study in the southeastern coastal area of China. *Nat. Hazards* **2025**, *121*, 2535–2564. [CrossRef]
3. Wei, R.; Shan, Y.; Wang, L.; Peng, D.; Qu, G.; Qin, J.; He, G.; Li, W. Clustered rainfall-induced landslides in Jiangwan Town, Guangdong, China during April 2024: Characteristics and controlling factors. *Remote Sens.* **2025**, *17*, 2635. [CrossRef]
4. Chen, X.; Yao, X.; Zhou, Z.; Tian, X.; Tao, T.; Li, Q.; Wen, Y.; Song, G. Mining-induced deformation and slope stability in steep mountainous areas based on InSAR monitoring and rock movement theory: A case study from southwestern China. *Remote Sens.* **2026**, *18*, 2008. [CrossRef]
5. Yuan, W.; Jing, B.; Xu, H.; Tang, Y.; Zhang, S. A dynamic early warning model for flash floods based on rainfall pattern identification. *Int. J. Disaster Risk Sci.* **2024**, *15*, 769–788. [CrossRef]
6. Young, A.; Bhattacharya, B.; Daniëls, E.; Zevenbergen, C. Integrating WRF forecasts at different scales for pluvial flood forecasting using a rainfall threshold approach and a real-time flood model. *J. Hydrol.* **2025**, *656*, 132891. [CrossRef]
7. Dahal, R.K.; Hasegawa, S.; Nonomura, A.; Yamanaka, M.; Dhakal, S. DEM-based deterministic landslide hazard analysis in the Lesser Himalaya of Nepal. *Georisk* **2008**, *2*, 161–178. [CrossRef]
8. Sala, G.; Lanfranconi, C.; Frattini, P.; Riva, G.; Crosta, G.B. Cost-sensitive rainfall thresholds for shallow landslides. *Landslides* **2021**, *18*, 2979–2992. [CrossRef]
9. Rademann, L.K.; da Silva Ribeiro, L.; Trentin, R.; de Souza Robaina, L.E. Evaluation of performance of different machine learning techniques for mapping landslide susceptibility associated with extreme rainfall events in southern Brazil. *Nat. Hazards* **2025**, *121*, 23103–23120. [CrossRef]
10. Liu, Y.-H.; Huang, J.-B.; Xiao, R.-H.; Fang, R.-K. Study on early warning model for regional landslides based on random forest in Fujian Province. *J. Eng. Geol.* **2022**, *30*, 944–955. (In Chinese)
11. Song, Y.; Cao, Y.-B.; Fan, W. Probabilistic early warning model for rainfall-induced landslides based on a Bayesian approach. *Chin. J. Rock Mech. Eng.* **2023**, *42*, 558–574. (In Chinese)
12. Mao, Y.; Qin, H.; Shang, Y.; Huang, Z.; Gao, Z.; Miao, D.; Kouhdaragh, M. Implementing an explored advanced and integrated deep random forest learning-based model to monitor enhanced landslide susceptibility mapping. *Nat. Hazards* **2025**, *121*, 15655–15677. [CrossRef]
13. Ashuli, A.; Singh, A.; Dhiman, N.; Niraj, K.C.; Dubey, C.S.; Shekhar, S.; Shukla, D.P. Integration of active tectonic index and geomorphic parameters for landslide susceptibility mapping in the Barak River basin. *Nat. Hazards* **2025**, *121*, 23845–23875. [CrossRef]
14. Huang, F.-M.; Chen, J.-W.; Fan, X.-M.; Huang, J.-S.; Zhou, C.-B. Logistic regression fitting of rainfall-induced landslide occurrence probability and continuous landslide hazard prediction modelling. *Earth Sci.* **2022**, *47*, 4609–4628. (In Chinese)
15. Peng, M.; Wu, Q.; Liu, L. Geometric design of a seismic array for local geological structure velocity tomography in the reservoir area of the lower Jinsha River. *J. Geophys. Eng.* **2025**, *22*, 1475–1490. [CrossRef]
16. Chang, Z.L.; Huang, F.M.; Jiang, S.H.; Zhang, Y.; Zhou, C.; Huang, J. Slope unit extraction and landslide susceptibility prediction using a multi-scale segmentation method. *Adv. Eng. Sci.* **2023**, *55*, 184–195. (In Chinese)

17. Reichenbach, P.; Rossi, M.; Malamud, B.D.; Mihir, M.; Guzzetti, F. A review of statistically based landslide susceptibility models. *Earth-Sci. Rev.* **2018**, *180*, 60–91. [CrossRef]
18. Huang, F.; Zeng, S.; Yao, C.; Xiong, H.; Fan, X.; Huang, J. Uncertainties of landslide susceptibility prediction modeling: Influence of different selection methods of non-landslide samples. *Adv. Eng. Sci.* **2024**, *56*, 169–182. (In Chinese)
19. He, W.C.; Zhao, J.S.; Lin, Y.L.; Chen, G.-P.; Li, K.; Yao, W.-L. Landslide susceptibility assessment in Weixin County based on evidence weight and support vector machine models. *Sci. Technol. Eng.* **2023**, *23*, 6350–6360. (In Chinese)
20. Wu, H.-Y.; Zhou, C.; Liang, X.; Yuan, P.-C.; Yu, L.-B. Assessment of landslide susceptibility mapping based on the XGBoost model: A case study of Yanshan Township. *Chin. J. Geol. Hazard Control* **2023**, *34*, 141–152. (In Chinese)
21. Sameen, M.I.; Pradhan, B.; Lee, S. Application of convolutional neural networks featuring Bayesian optimization for landslide susceptibility assessment. *CATENA* **2020**, *186*, 104249. [CrossRef]
22. Huang, F.; Teng, Z.; Guo, Z.; Catani, F.; Huang, J. Uncertainties of landslide susceptibility prediction: Influences of different spatial resolutions, machine learning models and proportions of training and testing datasets. *Rock Mech. Bull.* **2023**, *2*, 100028. [CrossRef]
23. Guo, F.; Lai, P.; Huang, F.; Liu, L.; Wang, X.; He, Z. Literature review and research progress of landslide susceptibility mapping based on a knowledge graph. *Earth Sci.* **2024**, *49*, 1584–1606. (In Chinese)
24. Yi, J.-S.; Cheng, Y.-J.; Xu, Y.; Yin, G.-L. Meteorological warning thresholds for regional landslide disasters in red-bed hills and low-mountain areas based on process rainfall. *Bull. Soil Water Conserv.* **2024**, *44*, 215–222. (In Chinese) [CrossRef]
25. Zhu, Y.C.; Li, Y.M.; Wei, S.H. A prediction model study on landslides in Nujiang Prefecture. *J. Yunnan Univ. Nat. Sci. Ed.* **2016**, *38*, 610–619. (In Chinese)
26. Monsieurs, E.; Dewitte, O.; Demoulin, A. A susceptibility-based rainfall threshold approach for landslide occurrence. *Nat. Hazards Earth Syst. Sci.* **2019**, *19*, 775–789. [CrossRef]
27. Palau, R.M.; Berenguer, M.; Hürlimann, M.; Sempere-Torres, D. Implementation of hydrometeorological thresholds for regional landslide warning in Catalonia (NE Spain). *Landslides* **2023**, *20*, 2039–2054. [CrossRef]
28. Sachinthaka, R.; Kalatehjari, R.; Brook, M.S. Evolution and critical evaluation of deterministic physically based rainfall-induced landslide susceptibility mapping: A mixed review. *Nat. Hazards* **2025**, *121*, 20795–20818. [CrossRef]
29. Lee, S.; Roh, M.; Jo, H.-W.; Joon, K.; Lee, W.-K. Machine learning-based rainfall-induced landslide susceptibility model and short-term early warning assessment in South Korea. *Landslides* **2025**, *22*, 2809–2827. [CrossRef]